Quantum holonomic phases of higher-dimensional parameter spaces

J. Loredo*, M. A. Broome, D. H. Smith and A. G. White

Centre for Engineered Quantum Systems, Centre for Quantum Computer and Communication Technology, and School of Mathematics and Physics, University of Queensland, 4072 Brisbane, QLD, Australia.

A key challenge in quantum computing is avoiding decoherence, so that the fragile quantum properties of a system are not lost to the surrounding environment. Holonomic phases, i.e. geometric and topological, can play an important role in bypassing decoherence. They provide a platform for fault-tolerant universal quantum computing based entirely on geometric phase transformations, called holonomic quantum computation [1]. Current candidates [2–4] for this approach rely on the robustness [5] of well known geometric phases in the Poincaré sphere parameter space. Here we expand upon this work by experimentally demonstrating holonomic phases in a six-dimensional parameter space of a two-qubit photonic system. We find that as the entanglement between qubits increases, the resulting holonomic phase becomes less affected by changes in the state evolution. At the point of maximal entanglement the holonomic phase becomes topological and most resilient to evolution changes. Our results motivate the pursuit of holonomic quantum computation enhanced by robust topological phases.

arXiv:1306.3370v1 [quant-ph] 14 Jun 2013

The evolution of a physical system can be seen as a trajectory in a parameter space. In general, this space is multi-dimensional and can exhibit rich geometric and topological structure. If a space has a trivial structure (e.g. simply-connected Euclidean space), then the result of a vector parallel-transported along an arbitrary curve will not differ from one parallel-transported along the "shortest" path connecting the same pair of points. The latter is not true in spaces with non-trivial structure and the difference is called holonomy.

A holonomy on a quantum system will manifest as a phase imparted on the quantum state. Distinguishing this phase from the well known dynamical phase is the notion of "memory" of a state's motion in the holonomic case. In contrast to dynamical phases, which are proportional to the accumulated mean energy of the evolution, holonomic phases are entirely determined by the geometry and topology of the relevant parameter space, and their value depends only on the specific trajectory undertaken in this space. It is in this sense that they contain some information or memory of the state's evolution.

When the quantum parameter space is simply connected, the holonomy is a continuous-valued—with respect to continuous deformations of the trajectory—geometric phase [6] and it depends on the space's curvature. On the other hand, discrete-valued topological phases [7, 8] appear when the parameter space is not simply-connected.

Holonomies have important applications in universal quantum computing, providing schemes that are inherently robust against decoherence, such as holonomic quantum computation, where matrix-valued geometric phase transformations, called non-Abelian (non-commuting) holonomies, perform single-qubit phase gates and two-qubit conditional phase gates. This scheme has received a great deal of attention due to its potential to overcome decoherence, and has recently been experimentally realised in different architectures [9, 10]. However, holonomic phases in quantum systems have only been demonstrated with single- [11, 12] or uncorrelated two-qubit [13] states, where the parameter space is just the Poincaré sphere.

Here we study the case of correlated two-qubit states, where trajectories can evolve in spaces with richer geometry that can also be non-simply-connected. In these systems, one can observe holonomies arising solely from the topological structure of the parameter space, hence the potential to enhance their resilience to state perturbations.

To better elucidate two-qubit holonomic phases, consider an arbitrary two-qubit pure state written in its Schmidt decomposition:

$$|\psi(0)\rangle = e^{-i\beta/2}\cos\frac{\alpha}{2}|n_a m_b\rangle + e^{i\beta/2}\sin\frac{\alpha}{2}|n_a^{\perp} m_b^{\perp}\rangle,$$

where $\alpha \in [0,\pi]$ and $\beta \in [0,2\pi]$ parametrise the Schmidt sphere [14] of a correlation space, and $|n_a m_b\rangle$, $|n_a^{\perp} m_b^{\perp}\rangle$ are orthogonal product states defining the Schmidt basis. If the state is not maximally entangled, there are preferred directions, $\vec{a}$ and $\vec{b}$, for qubits a and b respectively on their corresponding Poincaré spheres. These point towards the projections, for each qubit, of the more populated state in the Schmidt basis. Consequently, two parameters per preferred directions $\vec{a}$ and $\vec{b}$, and two more given by the Schmidt parameters α and β, are sufficient to uniquely define any non-maximally entangled two-qubit pure state. They span a six-dimensional parameter space.

*Electronic address: juan.loredo@uq.edu.au

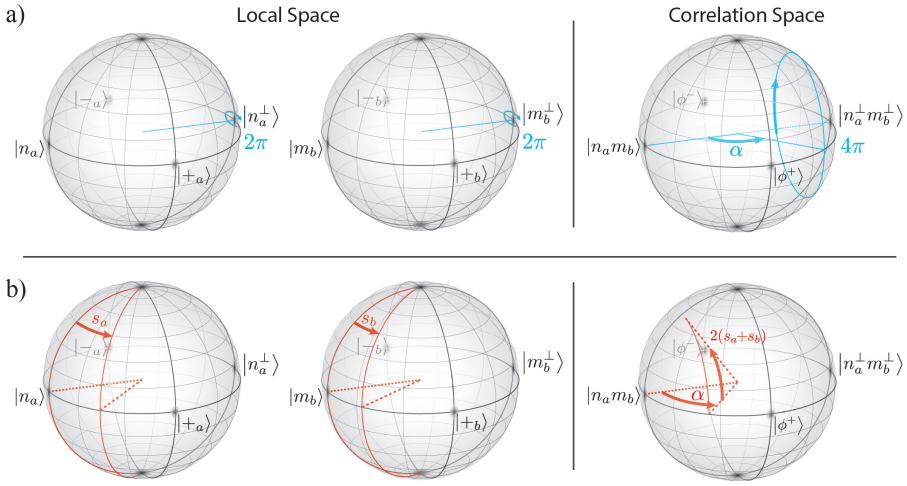

FIG. 1: **Evolutions of non maximally-entangled states.** Left and middle spheres show trajectories projected by the preferential directions of each qubit in their local space, i.e. Poincaré spheres defined in the initial Schmidt basis. Right spheres represent trajectories spanned by the evolution of α and β on the Schmidt sphere, whose axes do not remain constant and are defined by the instantaneous Schmidt basis. a) Evolution of a state around its preferred directions, in this case $|n_a^\perp\rangle, |m_b^\perp\rangle$, i.e. a Schmidt evolution. An evolution projecting onto single points in the local space encloses no area, and therefore no holonomic phase is gained as a result. However, a holonomic phase still arises as a result of the area enclosed by the curve in the correlation space. Equivalent Schmidt evolutions of separable states induce a zero holonomic phase. b) In contrast, an evolution not made around the preferred directions, in this case $|n_a\rangle, |m_b\rangle$, induce a holonomic phase appearing from both the local and correlation spaces. The parameters s_a and s_b define the opening angles of the projected curves in the local space and the rotation angle $2(s_a+s_b)$ around $|n_a m_b\rangle$ on the correlation space. Equivalent evolutions of separable states induce a non-zero holonomic phase.

While a treatment of the two-qubit space can be carried out formally [15], it is more intuitive to represent evolutions in it with the trajectories that $\vec{a}$ and $\vec{b}$ project onto their corresponding Poincaré spheres together with the curve that α and β project onto the Schmidt sphere, see Fig. 1.

Of particular interest are those trajectories that manifest a direct relationship between holonomic phases and the strength of quantum correlations. To illustrate this, we can define a "Schmidt evolution" as a 2π bi-local rotation of both qubits around $\vec{a}$ and $\vec{b}$, see Fig. 1a. The holonomic phase of this evolution can be calculated from the formula [16]

$$\Phi_{\rm h} = \arg\langle\psi(0)|\psi(\tau)\rangle - {\rm Im}\int_0^\tau \langle\psi(t)|\dot{\psi}(t)\rangle dt, \qquad (1)$$

where $\Phi_{\rm P}=\arg\langle\psi(0)|\psi(\tau)\rangle$ is the Pancharatnam [17] and $\Phi_{\rm dyn}={\rm Im}\int_0^\tau\langle\psi(t)|\dot{\psi}(t)\rangle dt$ is the dynamical phase, and $|\psi(t)\rangle, t\in[0,\tau]$ denoting the evolving state. This quantity, $\Phi_{\rm h}$, is usually identified as the geometric phase of the evolution. While this statement is true in the majority of cases, its explicit calculation reveals terms that do not occur due to the geometry (curvature) of the parameter space but rather due to, and only because of, its topology (connectedness). Such a distinction is not obvious in simple quantum systems, like single-qubit states, but is unambiguous in the case of composite ones. For instance, it has been shown that the parameter space containing all maximally-entangled two-qubit pure states (MES) can only induce a phase of topological origin [18].

Canonically, the amount of entanglement in a two-qubit state can be measured by the tangle $\mathbb{T}$ (concurrence squared [19]). In pure systems, it is determined by the relative populations of the Schmidt basis: $\mathbb{T} = \sin^2\alpha$, and ranges from 0 for separable states up to 1 for maximally-entangled states. Consequently, a Schmidt evolution will give rise to, see Appendix I for details, an entanglement-induced holonomic phase:

$$\Phi_{\rm h}^{\rm ent} = -2\pi\left(1-\sqrt{1-\mathbb{T}}\right). \qquad (2)$$

This shows that $\Phi_{\rm h}^{\rm ent}$ behaves monotonically with the amount of entanglement, ranging from 0 for separable states to -2π for MES; it is therefore a measure of quantum correlations of two-qubit pure states. While there are extensive theoretical studies of holonomic phases in entangled quantum systems [20–22], it remains an open question as to whether a similar expression holds true for mixed states.

The existence of a *holonomic phase of entanglement* implies we could use it as an entanglement-meter for two-qubit pure states if we were able to apply Schmidt evolutions to arbitrary states and measure only the $\Phi_{\rm h}^{\rm ent}$ gained in the evolution. Experimentally, however, it is the total Pancharatnam phase that is immediately observable [23]. By choosing evolutions such that the dynamical component vanishes, we can nevertheless ensure

the total phase gained to be holonomic, see Fig. 1b. The holonomic phase in this case is also monotonic with entanglement and is calculated as:

$$\Phi_{\rm h} = \mp \arctan\left(\sqrt{1-\mathbb{T}}\tan(2s)\right), \tag{3}$$

where the sign is $-$ $(+)$ if $|n_a m_b\rangle$ $(|n_a^{\perp} m_b^{\perp}\rangle)$ is the more populated state of the Schmidt basis, see Appendix II, and s defines the evolution undertaken by $|\psi(0)\rangle$. In our cases it is the opening angles, $s_a{=}s_b{=}s$, of the trajectories projected by $\vec{a}$ and $\vec{b}$ in their respective local spaces.

With increasing entanglement, separated points in the two-qubit parameter space become less distinguishable and when the entanglement is maximal some become identical, representing the same physical state. In this scenario the parameter space collapses from six to three dimensions and becomes the double-connected SO(3) ball [7, 8], see Fig. 2. This is a region of $\mathbb{R}^3$ whose border S^2_π—a two-dimensional sphere of radius π—has identified antipodal points. Spaces of this kind—not simply connected—allow trajectories that are topologically distinct, i.e. that cannot be smoothly transformed into one another, where the set of topologically equivalent trajectories defines a homotopy-class.

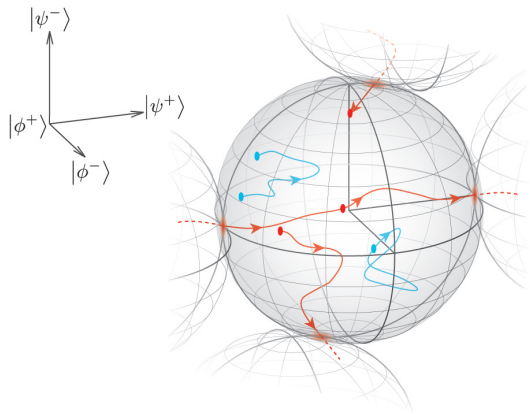

FIG. 2: **Evolutions of maximally entangled states.** Depiction of the double-connected parameter space of maximally entangled states. Its border is a 2-sphere of radius π with identified antipodal points. Blue trajectories represent arbitrary evolutions for one homotopy-class along which no phase is gained. Red curves represent evolutions of the other homotopy-class after which a π phase appears on the wave-function.

Trajectories in the SO(3) ball are classified by two different homotopy-class families: those that cross S^2_π an odd number of times and those crossing it an even number of times (zero included). The physical implication is that a trajectory crossing S^2_π l-times picks up an $l\pi$ phase. For instance, one can show that evolutions giving rise to equation (2) for maximal entanglement cross S^2_π twice, picking up a 2π topological phase.

Figure 3 shows our experimental scheme for measuring holonomic phases of two-qubit states given by equation (3). Our method works as follows: We generate two-qubit states encoded in the polarisation of single-photons whose tangle can be tuned from $\mathbb{T}{=}0{\to}1$ [24, 25]. The two photons described by the joint polarisation-state $|\psi\rangle$, travel through an interferometer, depicted in Fig. 3a. At the first 50:50 beam-splitter BS1, the photons are subject to non-classical interference [26], after which they exit via the same spatial mode (regardless of the specific form of $|\psi\rangle$ bunching can always be achieved by engineering other photon degrees of freedom if necessary [27]). This means that the joint state of the system, $|\psi\rangle$, remains in either of the two paths of the interferometer. The joint state then undergoes a polarisation evolution, composed of two auxiliary evolutions $\breve{U}$ and $\hat{U}$ in separate paths of the interferometer, such that both arms have the same optical path length.

Finally, the information about which-path the photons followed is erased by a second 50:50 beam-splitter BS2, after which point the photons are detected. As such, the two-photon coincidence signal, c, will exhibit interference behaviour modulated by all relative phases between the two arms of the interferometer. That is, caused by an optical path-difference phase ϕ and the Pancharatnam phase $\Phi_{\rm P}$ arising in the polarisation evolution.

We prepared the initial polarisation-entangled state $|\psi\rangle{=}\cos\frac{\alpha}{2}|HH\rangle + \sin\frac{\alpha}{2}|VV\rangle$, where α is a tuneable parameter defining the amount of entanglement, and $|H\rangle$ and $|V\rangle$ denote the horizontal and vertical polarisations. The state is injected into a displaced-Sagnac interferometer configuration, which exhibits inherent phase stability, shown in Fig. 3b. Using the notation $\sigma_1{=}|H\rangle\langle H|{-}|V\rangle\langle V|$ and $\sigma_2{=}|H\rangle\langle V| + |V\rangle\langle H|$, we choose an evolution

$$U \equiv \hat{U}^\dagger \breve{U} = e^{i\frac{\pi}{4}\sigma_2} e^{-i\frac{\pi}{2}(\sigma_1 \sin s + \sigma_2 \cos s)} e^{i\frac{\pi}{4}\sigma_2},$$

where s equals the opening angle of the corresponding trajectories in the local space, see Fig. 1b. Importantly, one can show that dynamical phases vanish along such trajectories, such that the total Pancharatnam phase matches the holonomic component from equation (1). The path-difference phase ϕ is introduced by slightly rotating one of the mirrors of the interferometer, see Fig. 3b. Recalling that the coincidence modulation will be given by $c{=}|e^{2i\phi}|\psi\rangle + (\hat{U}^\dagger\breve{U}\otimes\hat{U}^\dagger\breve{U})|\psi\rangle|^2/4$, it can thus be shown to vary as:

$$c = \frac{1}{2}\left[1 + v\cos(2\phi - \Phi_{\rm h})\right], \tag{4}$$

where $v{=}|\langle\psi|\psi'\rangle|$ is the interference visibility and $\Phi_{\rm h}{=}\arg\langle\psi|\psi'\rangle$ is the holnomic phase gained during the effective evolution $|\psi'\rangle{=}U{\otimes}U|\psi\rangle$. Consequently, we can measure the holonomic phase by measuring the phase offset in the coincidence signal modulation with respect to ϕ.

The chosen polarisation evolution is implemented using quarter- Q and half-wave plates H through

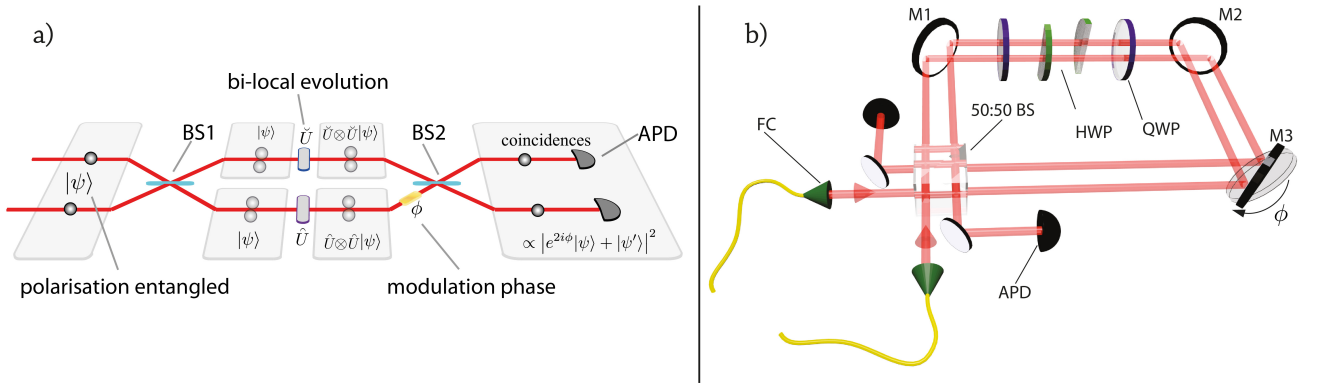

FIG. 3: **Experimental set-up to measure two-qubit holonomic phases.** a) Depiction of the experimental method. Two indistinguishable photons encoding a two-qubit entangled state $|\psi\rangle$ pass through an interferometer and are detected in coincidence with avalanche-photo-diodes (APD) at the output. Due to the Hong-Ou-Mandel effect at the first beam-splitter BS1, a coincidence signal c cannot distinguish between different paths travelled in the interferometer, and therefore shows the interference behaviour $c \propto |e^{2i\phi}|\psi\rangle + |\psi'\rangle|^2$. The Pancharatnam phase gained by an evolved state $|\psi'\rangle = \hat{U}^\dagger \breve{U} \otimes \hat{U}^\dagger \breve{U}|\psi\rangle$ appears as a phase-shift in the coincidence detection. The evolutions $\breve{U}$ and $\hat{U}$ are chosen to induce no dynamical phase, thus the Pancharatnam phase matches the holonomic phase. b) Experimental implementation of the method. Single photons are injected via single-mode fibre couplers (FC) into a displaced-Sagnac interferometer configuration, composed of one 50:50 beam-splitter BS and three mirrors M1-3. This is used for inherent phase stability so that no active phase locking is required. The geometry of the Sagnac configuration allows the implementation of the desired evolutions with two common-path quarter-wave plates QWP and two semi-circular half-wave plates HWP in separate optical paths. Mirror M3 is rotated via a micro-translation stage to control ϕ.

$U = Q(-\frac{\pi}{4})H(\frac{\pi}{4}-\frac{s}{2})Q(-\frac{\pi}{4})$, where the arguments of the wave plates indicate the angle of the optic axis in the laboratory frame. The respective auxiliaries are realised by $\breve{U} = Q(-\frac{\pi}{4})H(\frac{\pi}{4}-\frac{s}{4})Q(-\frac{\pi}{4})$ and $\hat{U} = Q(\frac{\pi}{4})H(-\frac{\pi}{4}-\frac{s}{4})Q(\frac{\pi}{4})$. Due to the geometry of our displaced-Sagnac interferometer we can perform the aforementioned evolutions using two common-path quarter-wave plates with angles fixed at $-\frac{\pi}{4}$ and two semi-circular half-wave plates, one in each path, at $\frac{\pi}{4}-\frac{s}{4}$ for $\breve{U}$ and $\frac{\pi}{4}+\frac{s}{4}$ for $\hat{U}$, see Fig. 3b.

Figure 4a shows our measured and predicted results for $\Phi_{\rm h}$ in a cyclic colour-scale, as a function of the degree of entanglement α and the opening angle s. Figure 4b shows in more detail that the bipartite holonomic phase of separable states, $\alpha=0$ (solid black curve) and $\alpha=\pi$ (dashed black curve), is simply the sum of individual geometric phases $\Phi_{\rm h}^{\rm sep} = \mp(s+s)$. Figure 4a shows that as the amount of entanglement increases, i.e. as $\alpha \to \pi/2$, the holonomic phase becomes less affected by increments of the opening angle s. That is, it becomes more resilient to changes in the evolution. Two attractors $\Phi_{\rm h}=0$ and $\Phi_{\rm h}=\pi$ appear and become the only possible values for a topological holonomic phase when the entanglement is maximum, i.e. $\alpha=\pi/2$. Solid- and dashed- blue curves in Fig. 4b show our measurements of the extent to which we observe a topological behaviour, for $\mathbb{T}=0.99 \pm 0.01$; the red lines show the ideal holonomic phase for $\mathbb{T}=1$. As discussed previously, the corresponding evolutions follow trajectories in the double-connected SO(3) space, thus giving rise to topologically distinct paths. Figure 4c shows the corresponding paths for five such evolutions, for which the point at $s=\frac{\pi}{4}$ represents the transition between two distinct homotopy-classes.

Experiments [28, 29] observing such topological phases have been realised with cyclic evolutions using classical states that are formally equivalent to a MES, corresponding to the top and bottom data points at $\alpha=\pi/2$ in Fig. 4a. In contrast, we demonstrated topological behaviour for explicitly non-cyclic evolutions, see Fig. 4c, of genuinely entangled quantum systems.

In contrast to conventional measurements of single-qubit holonomic phases [11, 12], the phase shift induced in our work is dependent on genuine quantum correlations. We find that the holonomic phase becomes more resilient to evolution changes with increasing entanglement, which indicates that quantum correlations can be utilised to enhance holonomic robustness and there may be advantages in using not only geometric but the full range of holonomic phases. Naturally, this leads to the question as to whether more general forms of quantum correlations—most notably discord [30]—could be the underlying reason for this enhancement. We expect that this work will strongly motivate new proposals for more robust holonomic quantum computation and trigger observations of holonomies in higher dimensions or n-fold entangled states of qubits or qudits.

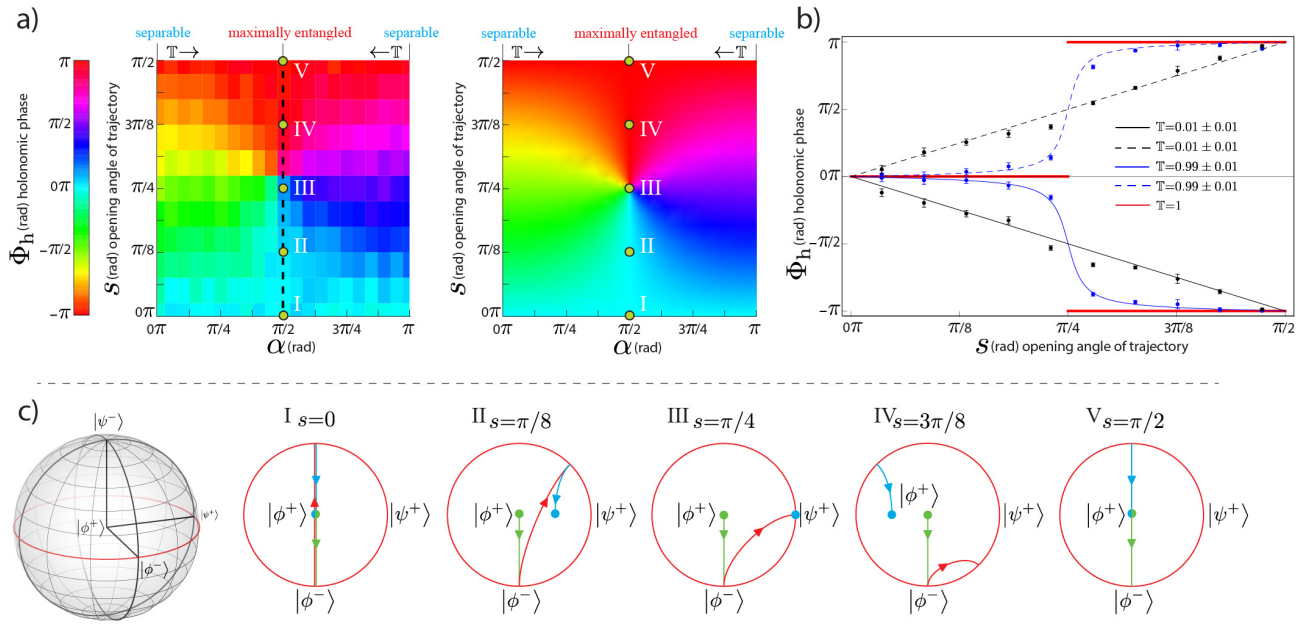

FIG. 4: **Experimental results.** a) Measured (left) and predicted (right) results for $\Phi_h = -\arctan(\cos(\alpha)\tan(2s))$ (equivalent to equation (3)). b) Black solid (dashed) curves show measurements of holonomic phases with a initial $|HH\rangle$ ($|VV\rangle$) state. Blue curves show the extent to which we observe a topological behaviour, ideally discrete red lines corresponding to $\mathbb{T}$=1, of the holonomic phase for a quasi-maximal entangled state slightly more populated in $|HH\rangle$ (solid curve) and $|VV\rangle$ (dashed curve). c) Depiction of cyclic (I,V) and non-cyclic (II,III,IV) evolutions of MES in the double-connected SO(3) ball. Green, red and blue coloured-curves denote the first, second and third part of each evolution, respectively.

Methods

The pair of polarisation entangled single-photons with a wavelength centred at 820 nm are produced via spontaneous parametric downconversion in a 10 mm custom-poled $KTiOPO_4$ (cpKTP) nonlinear crystal as described in ref. [24, 25]. They are injected into a displaced-Sagnac interferometer, depicted in Fig. 3b, with two counter-propagating modes displaced by $\sim$ 5 mm so that the semi-circular half-wave plates work in separate optical paths.

The path-difference phase ϕ is introduced by rotating a mirror mounted on a motorised stage capable of rotations in steps of $\sim 10^{-5}$ degrees. Complete cycles ($\phi \to 2\pi$) are obtained by rotations of the order $\sim 10^{-4}$ degrees. The dependence in 2ϕ of a coincidence signal, as in equation (4), has been reported, e.g. in ref. [13], and in our case is confirmed by a comparison with a 1ϕ-dependent modulation signal obtained with a one-photon input state.

The reference coincidence signal, i.e. for Φ_h=0, was obtained by imposing s=0 and averaging all phase offsets by varying α between α=0 and α=π in steps of $\Delta\alpha$=$\pi/20$. A maximum in the reference signal is equivalent to $\sim 12,000$ collected coincidence events. The experimental errors arise from instabilities, e.g. small mirror rotations ($< 10^{-5}$ degrees), to which the Sagnac interferometer is sensitive to and from Poissonian photon-counting statistics. Refer to the Appendix III for a more detailed presentation of the measured coincidence signal.

Although the presented data in this work was taken with indistinguishable photons inside the Hong-Ou-Mandel dip [26], qualitatively similar preliminary measurements were obtained with distinguishable photons given outside the dip, see Appendix III. However, given our particular evolutions, it can be shown that the "crossing terms", that are absent in the indistinguishable case do not contribute alter the measured phase offset. In this case they show up merely as a background of counts, reducing the overall signal-to-noise ratio and interference visibility.

Acknowledgments

We thank G. J. Milburn for stimulating discussions, and A. Fedrizzi, C. Branciard, I. Kassal and M. Ringbauer for critical feedback. This work was supported by: The Australian Research Council's Centre for Quantum Computation and Communication Technology (CE110001027), Centre for Engineered Quantum Systems (CE110001013), and Federation Fellow program (FF0668810).

References

[1] Zanardi, P. & Rasetti, M. *Phys. Lett. A* **264,** 94-99 (1999).
[2] Duan, L.-M., Cirac, J. I. & Zoller, P. *Science* **292,** 1695-1697 (2001).
[3] Wu, L.-A., Zanardi, P. & Lidar, D. A. *Phys. Rev. Lett.* **95**, 130501 (2005).
[4] Sjöqvist, E. et al. *New J. Phys.* **14,** 103035 (2012).
[5] Filipp, S. et al. *Phys. Rev. Lett.* **102,** 030404 (2009).
[6] Berry, M. V. *Proc. R. Soc. Lond. A* **392,** 45-57 (1984).
[7] Milman, P. & Mosseri, R. *Phys. Rev. Lett.* **90,** 230403 (2003).
[8] LiMing, W., Tang, Z. L. & Liao, C. J. *Phys. Rev. A* **69,** 064301 (2004).
[9] Abdumalikov Jr, A. A. et al. *Nature* **496,** 482-485, (2013).
[10] Feng, G., Xu, G. & Long, G. *Phys. Rev. Lett.* **110,** 190501 (2013).
[11] Kwiat, P. G. & Chiao, R. Y. *Phys. Rev. Lett.* **66,** 588-591 (1991).
[12] Ericsson, M. et al. *Phys. Rev. Lett.* **94,** 050401 (2005).
[13] Kobayashi, H., Ikeda, Y., Tamate, S., Nakanishi, T. & Kitano, M. *Phys. Rev. A* **83,** 063808 (2011).
[14] Sjöqvist, E. *Phys. Rev. A* **62,** 022109 (2000).
[15] Jakóbczyk, L. & Siennicki, M. *Phys. Lett. A* **286,** 383-390 (2001).
[16] Mukunda, N. & Simon, R. *Ann. Phys.* **228,** 205-268 (1993).
[17] Pancharatnam, S. *Proc. Ind. Acad. Sci. A* **44,** 247-262 (1956).
[18] Milman, P. *Phys. Rev. A* **73,** 062118 (2006).
[19] Hill, S. & Wootters, W. K. *Phys. Rev. Lett.* **78,** 5022-5025 (1997).
[20] Tong, D. M., Sjöqvist, E., Kwek, L. C., Oh, C. H. & Ericsson, M. *Phys. Rev. A* **68,** 022106 (2003).
[21] Ericsson, M., Pati, A. K., Sjöqvist, E., Brännlund, J. & Oi, D. K. L. *Phys. Rev. Lett.* **91,** 090405 (2003).
[22] *Phys. Rev. A* **85,** 032112 (2012).
[23] Loredo, J. C., Ortíz, O., Weingärtner, R. & De Zela, F. *Phys. Rev. A* **80,** 012113 (2009).
[24] Brańczyk, A., Fedrizzi, A., Stace, T., Ralph, T. & White, A. *Opt. Express* **19,** 55 (2011).
[25] Smith, D. H. et al. *Nat. Commun.* **3,** 625 (2012).
[26] Hong, C. K., Ou, Z. Y. & Mandel, L. *Phys. Rev. Lett.* **59,** 2044-2046 (1987).
[27] Walborn, S. P., de Oliveira, A. N., Pádua, S. & Monken, C. H. *Phys. Rev. Lett.* **90,** 143601 (2003).
[28] Souza, C. E. R., Huguenin, J. A. O., Milman, P. & Khoury, A. Z. *Phys. Rev. Lett.* **99,** 160401 (2007).
[29] Du, J., Zhu, J., Shi, M., Peng, X. & Suter, D. *Phys. Rev. A* **76,** 042121 (2007).
[30] Ollivier, H. & Zurek, W. H. *Phys. Rev. Lett.* **88,** 017901 (2001).

Appendix

I. Calculation of holonomic phase of entanglement

Consider the arbitrary initial two-qubit pure state written in its Schmidt decomposition

$$|\psi(0)\rangle = \cos\frac{\alpha}{2}e^{-i\beta/2}|n_a m_b\rangle + \sin\frac{\alpha}{2}e^{i\beta/2}|n_a^\perp m_b^\perp\rangle$$

subject to a rotation of both qubits around their preferential directions $\vec{a}$ and $\vec{b}$ in the corresponding Poincaré sphere. That is, a bi-local rotation $U^{\mathcal{S}}(\theta) = U_a^{\mathcal{S}(n)}(\theta) \otimes U_b^{\mathcal{S}(m)}(\theta)$ such that $U_j^{\mathcal{S}(k)}(\theta) = \exp\left(-i\theta\sigma_j^{(k)}/2\right)$, where θ is the angle of rotation, $\sigma_j^{(k)} = \eta|k_j\rangle\langle k_j| - \eta|k_j^\perp\rangle\langle k_j^\perp|$, and η is the sign of $\cos\alpha$. The holonomic phase of such evolution can be calculated from the formula

$$\Phi_{\rm h} = \arg\langle\psi(0)|\psi(\theta)\rangle - {\rm Im}\int_0^\theta \langle\psi(\theta')|\dot{\psi}(\theta')\rangle d\theta',$$

where $\Phi_{\rm P}=\arg\langle\psi(0)|\psi(\theta)\rangle$ is the Pancharatnam and $\Phi_{\rm dyn}={\rm Im}\int_0^\theta\langle\psi(\theta')|\dot{\psi}(\theta')\rangle d\theta'$ is the dynamical phase, giving

$$\begin{aligned}\arg\langle\psi(0)|\psi(\theta)\rangle &= \arg\left(\cos\theta - i\eta\cos\alpha\sin\theta\right)\\ &= \arg\left(\cos\theta - i|\cos\alpha|\sin\theta\right),\end{aligned}$$

and

$$\begin{aligned}{\rm Im}\int_0^\theta \langle\psi(\theta')|\dot{\psi}(\theta')\rangle d\theta' &= {\rm Im}\int_0^\theta -i\eta\cos\alpha d\theta'\\ &= -|\cos\alpha|\theta.\end{aligned}$$

We define a "Schmidt evolution" as $U^{\mathcal{S}}(\theta{=}2\pi)$, then

$$\begin{aligned}\Phi_{\rm h}^{\rm ent} &= \arg\left(\cos 2\pi - i|\cos\alpha|\sin 2\pi\right) + 2\pi|\cos\alpha|\\ &= \arg\left(e^{-i2\pi}\right) + 2\pi|\cos\alpha|.\end{aligned}$$

Using the expression for the tangle $\mathbb{T}{=}\sin^2\alpha$, we find the holonomic phase of entanglement to be

$$\Phi_{\rm h}^{\rm ent} = -2\pi\left(1-\sqrt{1-\mathbb{T}}\right).$$

II. Holonomic phase in evolutions with vanishing dynamical phase

In our experiment we prepare the initial polarisation-entangled state $|\psi\rangle{=}\cos\frac{\alpha}{2}|HH\rangle + \sin\frac{\alpha}{2}|VV\rangle$, where $|H\rangle$ and $|V\rangle$ denote horizontal and vertical polarisations. We choose bi-local evolutions $U\otimes U$, with

$$U = e^{i\frac{\pi}{4}\sigma_2}e^{-i\frac{\pi}{2}(\sigma_1\sin s+\sigma_2\cos s)}e^{i\frac{\pi}{4}\sigma_2},$$

where $\sigma_1{=}|H\rangle\langle H| - |V\rangle\langle V|$, $\sigma_2{=}|H\rangle\langle V| + |V\rangle\langle H|$ and s equals the opening angles of the trajectories projected

onto the Poincaré spheres. For this particular evolution, one can demonstrate that the dynamical phase vanishes at every step of the evolution. Then the holonomic phase is calculated as

$$\begin{aligned}\Phi_{\rm h} &= \arg\left(\cos 2s - i\cos\alpha\sin 2s\right)\\ &= -\arctan\left(\cos\alpha\tan 2s\right).\end{aligned}$$

Using $\cos\alpha{=}\eta\sqrt{1-\mathbb{T}}{=}\pm\sqrt{1-\mathbb{T}}$, where the sign is $+$ $(-)$ if $|HH\rangle$ ($|VV\rangle$) is more populated, we find that

$$\Phi_{\rm h} = \mp\arctan\left(\sqrt{1-\mathbb{T}}\tan(2s)\right).$$

For equally-populated states (maximally-entangled states) the sign is irrelevant and the holonomic phase $\Phi_{\rm h}{=}\arg(\cos 2s)$ is topological, being $\Phi_{\rm h}{=}0$ for $\cos 2s \geq 0$, and $\Phi_{\rm h}{=}\pi$ for $\cos 2s < 0$.

III. Coincidence signal

Ideally, two parameters, s and α, define the probability $c{=}\frac{1}{2}\left[1+v_{\rm t}\cos(2\phi-\Phi_{\rm h})\right]$, with $v_{\rm t}{=}\sqrt{(\cos 2s)^2+(\cos\alpha\sin 2s)^2}$ and $\Phi_{\rm h}{=}-\arctan\left(\cos\alpha\tan 2s\right)$, of detecting a coincidence event in the experimental set-up described in the main text. Then, if N pairs of single-photons enter the set-up, theoretically we would observe a coincidence signal

$$c_{\rm t} = \frac{N}{2}\left[1+v_{\rm t}\cos(2\phi-\Phi_{\rm h})\right],$$

which predicts a reference, i.e. $s{=}0$, theoretical visibility $v_{\rm t}^{\rm r}{=}\left(c_{\rm t}^{\rm r,max}-c_{\rm t}^{\rm r,min}\right)/\left(c_{\rm t}^{\rm r,max}+c_{\rm t}^{\rm r,min}\right){=}1,\ \ \forall\alpha,$ where max (min) stands for maximum (minimum) value with respect to ϕ.

Experimentally, however, neither the beamsplitter possesses a perfect 50:50 reflection/transmission ratio nor the photons are perfectly indistinguishable, this will cause the measured reference counts drop to a minimum of non-zero N_0 events. Accordingly, the maximum and minimum number of experimental reference counts, $c_{\rm e}^{\rm r,max}{=}N, c_{\rm e}^{\rm r,min}{=}N_0$, give an experimental reference visibility $v_{\rm e}^{\rm r} = (N-N_0)/(N+N_0)$. Then, the correction for the experimental coincidence signal is given by

$$c_{\rm e} = \frac{(N-N_0)}{2}\left[1+v_{\rm t}\cos(2\phi-\Phi_{\rm h})\right]+N_0, \qquad (5)$$

from where we can calculate the experimental visibility

$$v_{\rm e} = v_{\rm t}v_{\rm e}^{\rm r}, \qquad (6)$$

and, alternatively, write the experimental signal as

$$c_{\rm e} = \frac{(N+N_0)}{2}\left[1+v_{\rm e}\cos(2\phi-\Phi_{\rm h})\right],$$

with $0 \leq v_{\rm e} \leq (N-N_0)/(N+N_0)$. Figure 5 shows our recorded coincidence signals for four cases.

Our measurements outside the Hong-Ou-Mandel dip and a qualitatively comparison with the corresponding data inside the dip are shown in figure 6.

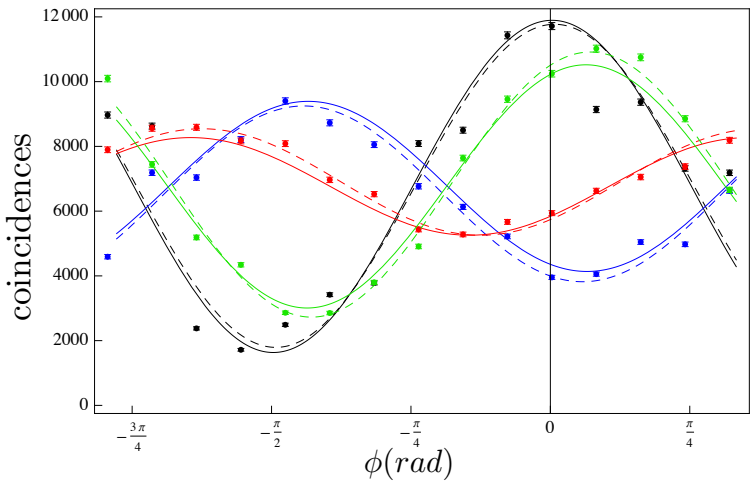

FIG. 5: **Counted coincidence events.** The reference signal (solid black curve) was obtained from finding N^i and N_0^i by imposing s^i=0 and α^i=$i\pi/20, i = 0, 1, ..., 20$ and averaging them to obtain N=11911 and N_0=1616, the phase origin, i.e. ϕ=0, is set to be the average of their phases. Black points and dashed black curve represent the collected coincidence counts and best sinusoidal fit for (s, α)=$(0, \frac{8}{20}\pi)$. Blue, red and green points and curves correspond to the predicted experimental coincidence signal (solid curves) c_e, see Eq. (5), and best sinusoidal fits (dashed curves) for (s, α)=$(\frac{7}{10}\frac{\pi}{2}, \frac{8}{20}\pi)$, (s, α)=$(\frac{6}{10}\frac{\pi}{2}, \frac{11}{20}\pi)$ and (s, α)=$(\frac{3}{10}\frac{\pi}{2}, \frac{12}{20}\pi)$, respectively.

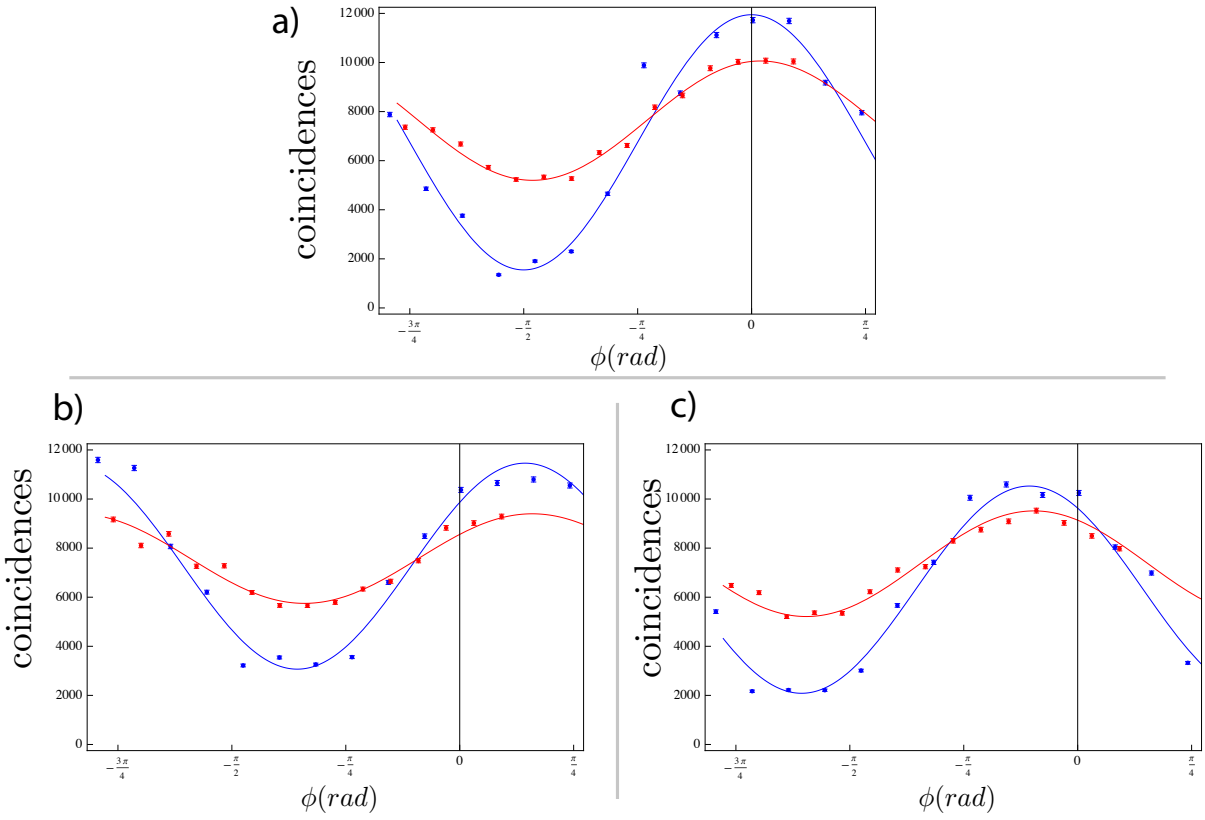

FIG. 6: **Indistinguishable-distinguishable cases comparison.** Counted coincidences inside (blue dots) and outside (red dots) the Hong-Ou-Mandel dip for a) (s, α)=$(0, \frac{9}{20}\pi)$, b) (s, α)=$(\frac{4}{10}\frac{\pi}{2}, \frac{14}{20}\pi)$ and c) (s, α)=$(\frac{3}{10}\frac{\pi}{2}, \frac{3}{20}\pi)$. Curves represent best sinusoidal fits for the corresponding data. Inside and outside the dip we obtain N=11911, N_0=1616, and N^{out}=10000, N_0^{out}=5068, respectively. Which, from Eq. (6), predicts an outside/inside visibility ratio of 0.43. The observed visibility ratios are 0.41, 0.42 and 0.44 for a), b) and c), respectively.